RSC Advances

PAPER

View Article Online
View Journal | View Issue

Cite this: *RSC Adv.*, 2014, **4**, 29107

Supported Ni–La–O_x for catalytic decomposition of N_2O I: component optimization and synergy

Chengliang Li, Yuesong Shen,* Shemin Zhu* and Shubao Shen

Received 18th March 2014
Accepted 17th June 2014

DOI: 10.1039/c4ra02386b

www.rsc.org/advances

A series of Ni–La–O_x complex oxides with Ni/La integer molar ratios from 1 to 10 supported on pretreated cordierite ceramics were prepared by an impregnation method and tested for direct catalytic decomposition of N_2O. The Ni–La–O_x complex oxides showed considerable synergy in N_2O decomposition compared with pure nickel oxide, and the supported Ni–La–O_x complex oxides exhibited much better catalytic performance in reactions. The promotional effects of material structure and synergy of Ni- and La-based oxides on catalytic performance for N_2O decomposition were systematically studied through characterization by XRD, N_2-BET, H_2-TPR, N_2O-TPD and XPS. The results show that the NiO and $LaNiO_3$ are major active solid-phases for catalytic decomposition of N_2O; the synergetic action between NiO and $LaNiO_3$ promotes oxygen mobility and desorption, and stabilizes the active site of Ni^{II}. Furthermore, a new reaction mechanism for N_2O decomposition over the supported Ni–La–O_x catalysts is proposed.

1. Introduction

Nitrous oxide (N_2O) is a long-lived trace gas, its atmospheric residence time is up to 100–200 years, and its annual growth rate is 0.2–0.3%.[1–4] N_2O exhibits a harmful global warming potential (GWP) 310 times higher than CO_2.[4–6] The continuous increase of atmospheric N_2O concentration not only caused global warming but also destroyed ozone layer with a subsequent increase in the amount of solar UV-B radiation reaching the earth.[6,7] Therefore, how to effectively control and remove N_2O has become a major environmental issue of worldwide common concern.

Major N_2O emission sources are including agricultural soil mining, industrial production of adipic acid, nitric acid and fertilizer, chemical processes using nitric acid as oxidant, coal combustion in fluidized bed, vehicle emissions, and byproduct formation in NH_3-SCR of NO_x *etc.*, correspondingly current treatment methods of N_2O are mainly including thermal decomposition, direct catalytic decomposition, SCR, and as a raw material for producing phenol and nitric acid.[4,8,9] Among them, the direct catalytic decomposition method, with merits of relatively low reaction temperature, no reductant consumption, low operating costs, and similar air component decomposition products of N_2 and O_2, has been regarded as the most promising technology for N_2O removal.[4,10]

As the technological core of the catalytic decomposition method, catalyst has been attracting wide attention. Various catalysts such as noble metals including Ru and Rh *etc.*,[11–15] metal oxides including Co_3O_4, CuO and Fe_3O_4 *etc.*,[16–21] supported metal oxides including Fe_2O_3/Al_2O_3, CoO/Al_2O_3 and NiO/mullite *etc.*,[22–26] ion-exchanged zeolites including ZSM-5, ZSM-11 and USY *etc.*,[27–32] and hydrotalcites[33–35] are being evaluated for catalytic decomposition of N_2O. Although the noble metal catalysts exhibit excellent catalytic performance at low temperature, only a few of them are active and stable enough for N_2O decomposition under industrial conditions, because their catalytic activities are seriously inhibited by O_2, NO and H_2O. Moreover, oxygen atoms formed by N_2O decomposition may cause catalyst deactivation.[36] In addition, the noble metals are very expensive and their thermal stabilities are poor in the higher temperatures.[37] Anyway, the noble metals are not suitable for large-scale industrial applications. The zeolite catalysts exhibit higher decomposition rate of N_2O at higher temperatures, while sulfates are easily formed on the surface of the zeolite, consequently resulting in catalytic activity decrease.

Development of catalysts for N_2O decomposition aims at the achievements of high catalytic activity, outstanding anti-poisoning ability and long-term cyclic stability at the lower temperature. The reaction mechanism of N_2O decomposition with the catalysts is generally considered as a charge donation from catalyst to the anti-bonding orbital of N_2O, consequently weakening the N–O bond and decomposing N_2O.[17] The removal of adsorbed oxygen is the rate-determining step for such a reaction. Hence, the improvement of the oxygen storage capacity and mobility is urgently required in the reaction.[38] Catalysts doped with rare-earth oxides often affect the mobility of oxygen on their surfaces. Russo *et al.*[39] studied several $LaBO_3$ (where B is Cr, Mn, Fe, and Co) perovskite-type oxides prepared

---

College of Materials Science and Engineering, State Key Laboratory of Materials-Oriented Chemical Engineering, Nanjing Tech University, No. 5, Xinmofan Road, Nanjing 210009, P.R. China. E-mail: sys-njut@163.com; Tel: +86-25-83587927

via solution combustion synthesis, and reported that the $LaCoO_3$ showed the best activity, with 50% N_2O conversion at 728 K and 763 K in the absence and presence of 5% of oxygen, respectively. Before this work, we have made a survey of various mixed metal oxide catalysts for N_2O decomposition, and found that most researches were concentrated on cobalt-based or copper-based catalysts because of their excellent catalytic activities.[18,19,21,40–43] Xue *et al.*[17] reported that the addition of CeO_2 into the Co_3O_4 catalyst could promote catalytic activity, and the $CoCe_{0.05}$ exhibited full N_2O conversion at 563 K. Asano *et al.*[18] reported that a potassium-doped Co_3O_4 catalyst, with the K/Co molar ratio of 0.02, obtained full conversion of N_2O at 573 K. Zhou *et al.*[21] reported that a $Cu_{0.67}Ce_{0.33}O_y$ catalyst exhibited the full N_2O conversion at 698 K. As mentioned above, a large number of investigations on catalyst for N_2O decomposition were concentrated on pure active components, particularly in powder scale. Anyway, development of a catalyst that is able to apply in real gas streams is one of the great challenges in N_2O emission control. As studied by Kapteijn *et al.*,[8] supported metal oxides were not as frequently studied as pure mixed oxides, but for industrial applications the supported metal oxides might be better suited due to their higher dispersion and low cost. However, the catalytic activities of the metal oxides would significantly decrease when they were loaded on carriers for industrial applications. For instance, the full N_2O conversions of the Fe_2O_3/Al_2O_3 and CoO/Al_2O_3 reached at 1023 K and 833 K,[25,26] respectively. Thereby how to improve the catalytic activity of the supported metal oxides at lower temperatures has become the most important scientific problem.

Besides Co- and Cu-based oxide catalysts, nickel-based oxide catalysts also exhibit good catalytic performance for N_2O decomposition, especially for the supported Ni-based oxide catalyst. Lan *et al.*[44] reported that a supported catalyst of NiO/mullite showed full N_2O conversion at 753 K. Wang *et al.*[45] studied a catalyst of Ni–Co–O_x supported on the modified cordierite honeycomb ceramic support, the results also indicated that the catalyst showed good catalytic activity and stability in N_2O decomposition. As stated above, the supported Ni-based oxide catalysts are promising for N_2O decomposition at lower temperature. In this work, a novel supported catalyst of Ni–La–O_x complex oxide, with a pretreated cordierite honeycomb ceramic as carrier, was systematically studied for N_2O decomposition in order to obtain the full N_2O conversion at much lower temperature. Moreover, the promotional effects of material structure and synergy of Ni- and La-based oxides on catalytic performance for N_2O decomposition were mainly studied.

2. Experimental

2.1 Catalyst preparation

A series of Ni–La–O_x complex oxides with 1–10 Ni/La integer molar ratio was prepared by thermal decomposition of Ni–La nitrate solution, which was made of $Ni(NO_3)_2$ (Xilong Chemical Co., Ltd, AR 98%) and $La(NO_3)_3$ (Sinopharm Chemical Reagent Co., Ltd, AR 99.8) under vigorous stirring at room temperature for 3 h. Then the Ni–La nitrate solution was dried at 333 K for 12 h in air, followed by calcination at 823 K for 2 h. The obtained Ni–La–O_x complex oxides were thus referred to as Ni_xLa (x stands for the molar ratio of Ni/La).

2.2 Preparation of supported catalysts

In order to simulate real monolith catalysts for industrial applications and reduce the amount of metal oxide active component, some pretreated cordierite honeycomb ceramics without catalytic ability (as shown in Fig. 2) were crushed into the particle sizes of 6–10 mesh to load uniformly dispersed Ni–La–O_x complex oxides by impregnation method. Ceramic pretreatment *via* acid pickling technology was washing with boiling 10 wt% HNO_3 solutions, and acid pickling temperature was 373 K while the duration time was 30 min. Then the ceramics were washed by distilled water until the pH was neutral, followed by dried at 353 K for 24 h. Subsequently the treated ceramics were immersed into the Ni–La nitrate solution for 1 h, then the supported catalysts were obtained about 10% mass loading amount of Ni–La–O_x complex oxides by drying at 333 K for 3 h, followed by calcination at 823 K for 2 h. The supported catalysts are referred to as S–Ni_xLa (x indicates the Ni/La molar ratio).

2.3 Characterization techniques

The X-ray diffraction (XRD) patterns were recorded in the 2-theta from 10° to 80° ($0.6^\circ\ min^{-1}$) using X-ray diffractometer (Rigaku DMAX-RB) with a radiation of Cu Kα ($\lambda = 1.5406$ Å). The crystal phases were confirmed according to the JCPDS reference. The unit cell parameters were calculated by refining the peak positions of the XRD patterns with a least squares refinement method using the CELREF program.[46] The JADE 6.5 program was used to determine peak positions.

The environmental scanning electron microscopy (ESEM) experiment was carried out on a JEOL (JSM-5900, Japan) instrument using 10 kV acceleration voltages to determine the morphology and particle size of the Ni_4La sample.

The textural properties of the Ni_xLa samples were evaluated from the liquid N_2 adsorption–desorption isotherms obtained at 77 K over the whole range of relative pressures, using a Micromeritics ASAP 2020 automatic equipment on samples previously outgassed at 473 K for 2 h. The Brunauer–Emmett–Teller (BET) method was performed to estimate the specific surface area of the Ni_xLa samples. Total pore volumes were determined using the *t*-plot method, and average pore diameter distributions were derived using the BJH method.

The hydrogen temperature-programmed reduction (H_2-TPR) profiles were obtained on a semiautomatic Micromeritics TPD/TPR 2900 apparatus. The samples were pre-treated, before the reduction measurement, at 423 K for 0.5 h in a helium flow, and then cooled to 323 K. Reduction profiles were obtained by passing a 10% H_2/Ar flow at a flow rate of 50 mL min^{-1} through the sample around 30 mg. The temperature was increased from 323 K to 1173 K at a rate of 5 K min^{-1} and the amount of hydrogen consumed was determined as a function of the temperature.

The selected NiLa, Ni_2La, Ni_4La, Ni_6La, Ni_8La and $Ni_{10}La$ samples were analyzed by the temperature-programmed desorption of N_2O (N_2O-TPD). The samples consisted of solid particles in 25–40 mesh range. Prior to N_2O-TPD, the samples around 100 mg were exposed to 30 mL min^{-1} of helium held at 823 K (10 K min^{-1}) for 1 h, then switched to N_2O flow (30 mL min^{-1}) and isothermal treatment at this temperature for 0.5 h, followed by cooling down to 323 K in N_2O flow. Afterwards, helium was fed to the reactor at 10 mL min^{-1} flow and kept flowing for 0.5 h in order to remove any excess oxygen species. The sample was then heated up to 873 K (10 K min^{-1}) under helium flow (10 mL min^{-1}), O_2 desorbed during the heating was recorded with the change of temperature.

The X-ray photoelectron spectroscopy (XPS) experiments were carried out on a RBD upgraded PHI-5000C ESCA system (Perkin Elmer) with Mg Kα radiation ($h\nu = 1253.6$ eV) or Al Kα radiation ($h\nu = 1486.6$ eV). In general, the X-ray anode was run at 250 W and the high voltage was kept at 14.0 kV with a detection angle at 54°. The pass energy was fixed at 23.5, 46.95 or 93.90 eV to ensure sufficient resolution and sensitivity. The base pressure of the analyzer chamber was about 5×10^{-8} Pa. The sample was directly pressed to a self-supported disk (10 × 10 mm) and mounted on a sample holder then transferred into the analyzer chamber. The binding energies of Ni 2p, La 3d and O 1s core levels were determined, referencing to the binding energy of adventitious C 1s signal at a binding energy of 284.6 eV, which gives an accuracy of ±0.1 eV. The data analysis was carried out by using the RBD AugerScan 3.21 software provided by RBD Enterprises and XPSPeak4.1 provided by Raymund W. M. Kwok (The Chinese University of Hong Kong, China). A standard Shirley background and Gaussian (*Y*%)–Lorentzian (*X*%) were used for each component.

2.4 Activity measurement and intrinsic kinetic evaluation

The activity measurements were carried out in a fixed-bed reactor using 5 mL catalysts as shown in Fig. 1. The inner diameter of the quartz tube reactor was 10 mm. The S–Ni_xLa samples were placed into the quartz reactor for catalytic decomposition of 5000 ppmv N_2O in reaction temperature range of 523–723 K (50 K per each testing temperature) at GHSV of 2400 h^{-1}. The concentrations of N_2O at the outlet of reactor were analyzed online by a gas chromatography (Shimadzu GC 2014) equipped with thermal conductivity detector (TCD) and Porapac Q column after 20 min reaction at each temperature.

The catalytic activity of S–Ni_xLa samples were evaluated in terms of N_2O conversion (X_{N_2O}) according to following equation:

$$X_{N_2O} = \frac{(X_{N_2O_{in}} - X_{N_2O_{out}})}{X_{N_2O_{in}}} \times 100\% \tag{1}$$

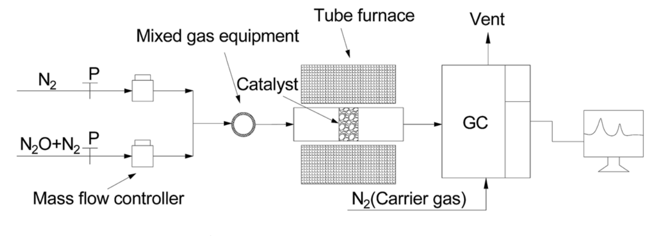

Fig. 1 The diagram of catalytic activity test system.

The decomposition of N_2O was confirmed to be the first-order in N_2O and zero-order in O_2 concentration.[47] The first-order rate (*k*), the apparent activation energy (E_{app}), and the turnover frequency (TOF) were calculated according to the following equations reported in ref. 48 and 49:

$$k = \frac{-\ln(1 - X_{N_2O})F}{m_{cat}P} \tag{2}$$

$$E_{app} = \frac{\partial(\ln k)}{\partial(1/T)} \tag{3}$$

$$\text{TOF}\ (s^{-1}) = \frac{kP_{N_2O}}{N} \tag{4}$$

where *F* is total flow rate (mol s^{-1}), m_{cat} is the amount of active phase (g), *P* is the total pressure (bar), P_{N_2O} is the partial pressure of N_2O (bar), and *N* is the active site (total cationic ions) content on active phase (mol g^{-1}).

The specific reaction rate (r_s, mol s^{-1} g^{-1} bar^{-1}) and the intrinsic reaction rate (r_i, mol s^{-1} m^{-2} bar^{-1}) were calculated according to as reported in ref. 50. F_{N_2O} is the N_2O molar flow rate at the inlet of the reactor.

$$r = k\frac{F_{N_2O}(1 - X_{N_2O})}{F} \tag{5}$$

Intrinsic kinetic was estimated using only data corresponding to N_2O conversion between 10% and 30%. Furthermore, the Koros–Nowak test[51] was performed over S–Ni_4La sample with the result verifying that the reaction conditions applied in the present work were located in the kinetic regime. The Koros–Nowak criterion for this reaction according to the following equations:

$$\rho = F/m_{cat}f_m \tag{6}$$

where ρ is defined as the active space velocity (ASV) and f_m is the concentration of the active materials (g of active material per g of catalyst). If the value of f_m is changed but ρ and N_2O conversion is invariant for two experiments, then the Koros–Nowak criterion is obeyed.

3. Results and discussion

3.1 Catalytic activity results

Fig. 2 shows the profile of N_2O conversion *versus* temperature over S–Ni_xLa samples. The pure NiO supported catalyst with the same mass loading amount and particle size as those of the S–Ni_xLa catalysts was tested for catalytic decomposition of N_2O in order to deeply reveal synergy of the Ni- and La-based oxide components in reaction. The activity of the pure NiO supported catalyst was low, and its N_2O conversion at 723 K was less than 30%. The doping of La generated more oxygen vacancies than bulk NiO catalyst on the surface of sample, and has a

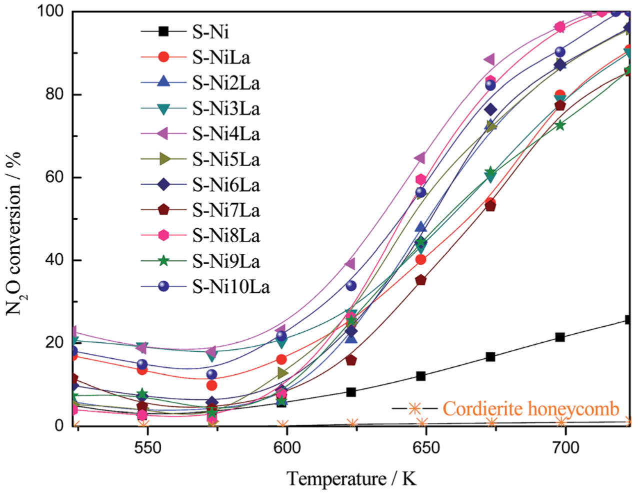

Fig. 2 Conversion of N_2O over supported Ni_xLa catalysts with different Ni/La ratios. Conditions: 5000 ppm N_2O, balance N_2, GHSV = 2400 h^{-1}.

Table 1 The specific metal content and the catalyst amount of the S–Ni_4La catalyst during the Koros–Nowak test

Samples	Metal content (wt%)	Catalyst amount (g)
S–Ni_4La-10%	10.4	3.65
S–Ni_4La-12%	12.6	3.01

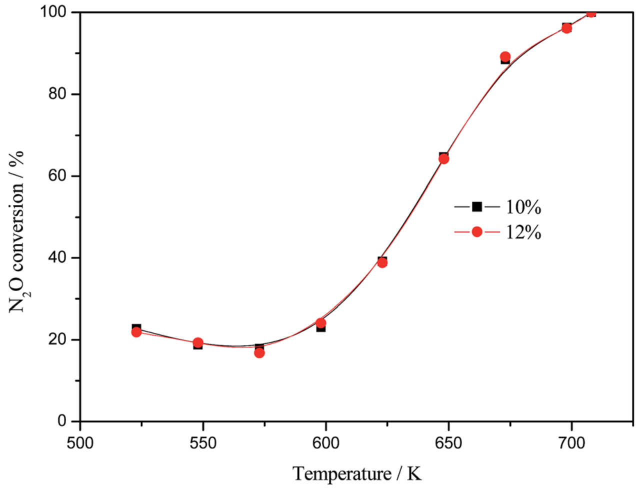

Fig. 3 Koros–Nowak tests for S–Ni_4La-10% and S–Ni_4La-12% samples.

promotional effect on the catalytic activity. Thus, the S–Ni_xLa catalysts exhibit better catalytic activity than bulk NiO supported catalyst. Compared with the catalytic performance of the pure NiO supported catalyst, the treated cordierite honeycomb ceramics exhibited almost no activity in reaction. It illustrates that herein the cordierite ceramics only play the role of loading and dispersing active Ni_xLa while have no effect on catalytic decomposition of N_2O. So the effect of the treated cordierite ceramics on catalytic performance will be ignored in the following analysis and discussion.

The S–Ni_xLa catalysts showed slight loss of activity in the temperature of 523–573 K. This loss may be related to physical adsorption of N_2O before 573 K in the heating process while no such phenomenon occurred in cooling process. This idea is supported by the Weber *et al.*'s study.[52] The total activity increased with increasing reaction temperature, particularly in temperature range from 573 K to 723 K. However, the actual catalytic activities of the S–Ni_xLa catalysts were different to each other with increasing La content in the series. The N_2O was decomposed completely at the lowest temperature of 708 K, which was obtained by the S–Ni_4La catalyst. The catalytic activity of S–Ni_4La and S–Ni_8La samples were 88.4% and 83.2% at the temperature of 673 K, respectively. However, the catalytic activities were almost same for S–Ni_4La and S–Ni_8La samples at 698 K. This may be due to the crystallite size of NiO in S–Ni_8La sample is smaller than S–Ni_4La sample. N_2O completely decomposition for S–Ni_8La catalyst obtained at 713 K, which is higher than S–Ni_4La sample. This indicated that the crystallite size is not the determining factor for catalytic activity.

In the heterogeneous catalytic reaction, it is well known that the mass transfer limitations play an important role on the reaction rate.[53] The heat- and mass-transfer limitations may be appeared during the reaction kinetic test. For this reason, the Koros–Nowak test was carried on 10 wt% and 12 wt% S–Ni_4La samples, respectively (Table 1). Fig. 3 shows the N_2O conversion over 10 wt% and 12 wt% S–Ni_4La samples. It is clearly observed that the reaction obeyed the Koros–Nowak criterion, which demonstrated that our present work are not affected by the heat- or mass-transfer limitations and located in the kinetic regime.

Considering that the real metal oxides loadings for the S–Ni_xLa samples were different, the intrinsic kinetic parameters (rate constant, reaction rate and turnover frequency) were compared as interpreted in Fig. 4. The intrinsic reaction rates and rate constants of N_2O decomposition are depicted as a function of $1/T$ (Arrhenius plots, Fig. 4a and b). It can be seen that per m^2 of Ni_4La surface area was able to convert the largest number of N_2O at per unit time, indicating that the S–Ni_4La possesses the highest N_2O conversion rate. Moreover, the effect of the Ni/La molar ratio on the reaction rate was not promoted as the Ni/La molar ratio increased. It implies that the interaction between Ni- and La-based oxide components plays key role in reaction; more or less La additives in S–Ni_xLa may be not helpful for N_2O decomposition.

The turnover frequency (TOF) values for the S–Ni_xLa catalysts are presented in Fig. 4c as a function of T. The results clearly demonstrate that per molar cationic ions of S–Ni_4La catalyst was able to convert the largest molar number of N_2O at per unit time, further indicating that the S–Ni_4La possesses the best catalytic performance.

For better comparison of their catalytic performances, the intrinsic kinetic parameters have been tentatively calculated at 610 K. The calculation results of the kinetic parameters are listed in Table 2. More obvious comparisons can be obtained

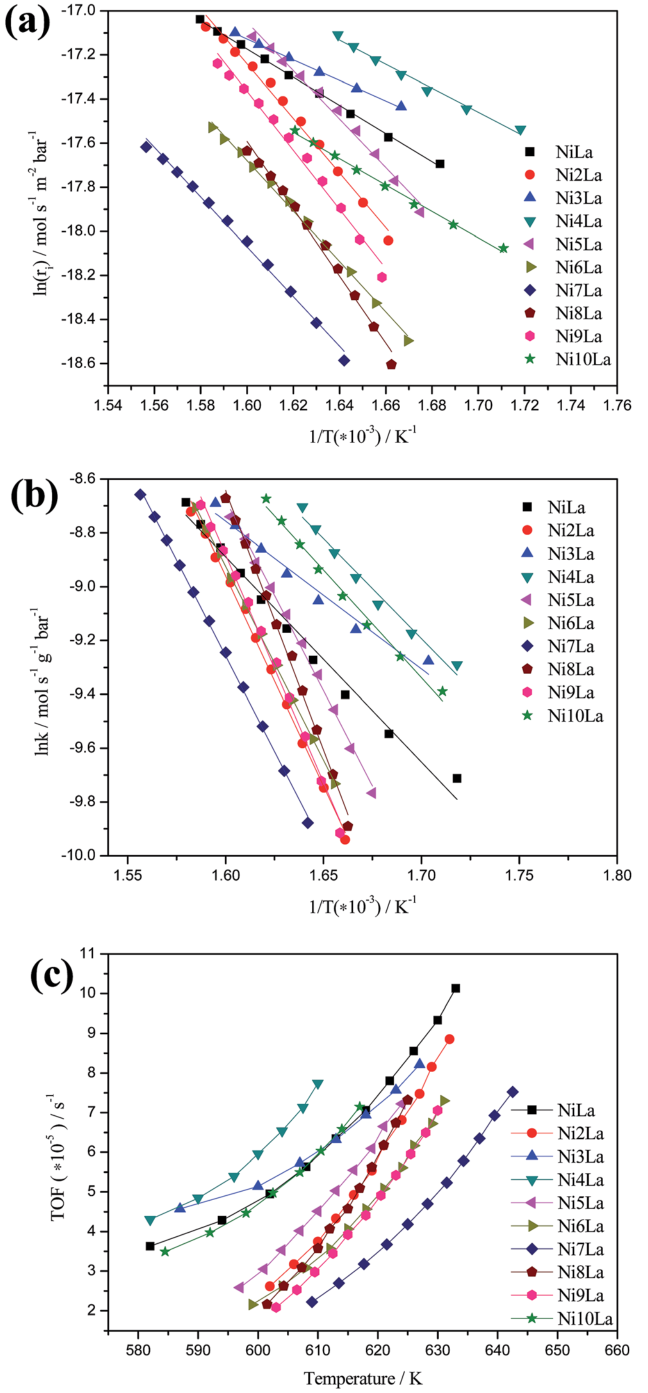

Fig. 4 (a) Arrhenius plots ln r_i *versus* 1/*T* over the S–Ni$_x$La samples; (b) Arrhenius plots ln *k versus* 1/*T* over the S–Ni$_x$La samples; (c) turnover frequencies (TOF) of the N_2O decomposition over the S–Ni$_x$La samples. N_2O direct decomposition *versus* reaction temperature corresponding to the N_2O conversion between 10% and 30%.

from the reaction rate values expressed per m^2 (per g) which led to the highest value on S–Ni$_4$La catalyst. In addition, the TOF shows that the S–Ni$_4$La catalyst had the highest values. By the comparison, the reaction rates of S–Ni$_x$La samples were higher than those values reported in the literature. This may be due to that the mobility of oxygen species on the Ni$_x$La surface is more easily.

The apparent activation energies on S–Ni$_x$La samples were all less than 150 kJ mol^{-1}, which were smaller than 177 kJ mol^{-1} reported in the literature. These values are lower than the energy requires to break the N–O bond in the N_2O molecule without catalyst participation (250–270 kJ mol^{-1}), which requires about 898 K.[54] Therefore, through above intrinsic kinetic evaluations, it can be found that the S–Ni$_4$La reveals a maximum synergetic effect between Ni- and La-based oxide components in reaction.

3.2 Textural characteristics

Table 2 lists The BET specific surface areas of the Ni$_x$La samples. The BET values range from 14.8 m^2 g^{-1} to 27.4 m^2 g^{-1}. The S–Ni$_8$La catalyst does not exhibit the optimal catalytic activity, even though it has the biggest specific surface area 27.4 m^2 g^{-1}. According to comparative analysis of specific surface area and catalytic activity, there is no direct relationship between their change trends. On the other words, the specific surface area is not the sole determining parameter here.[16,18] Meanwhile, there is also no direct relationship between catalytic activity and total pore volume as shown in Fig. 5. However, it can be found that the Ni$_4$La possesses the smallest average pore diameter about 17.4 nm, which may be the most appropriate size for mass transfer channel in reaction.

3.3 XRD analysis

Fig. 6 shows the X-ray diffractograms of the Ni$_x$La and pure NiO powders calcined at 823 K before reaction. All the reflections of the Ni$_x$La samples provide typical diffraction patterns for the cubic NiO (PDF 47-1049, marked as ▼) and perovskite-type $LaNiO_3$ (PDF 34-1181, marked as ●). Decreased intensity was observed in the reflections from cubic NiO with increased La concentration in the samples. Compared to the diffraction peaks of pure NiO sample, the NiO diffraction peaks of the Ni$_x$La samples were wider, indicating that the La additives minimize the crystal size of NiO. The formation of $LaNiO_3$ structure means that the part of Ni^{II} was oxidized into Ni^{III}, and the size of the Ni^{III} cation (0.62 Å) is smaller than that of the La^{III} cation (1.06 Å) inside the La_2O_3 structure, implying that the presence of $LaNiO_3$ perovskite structure could significantly promote the mobility of oxygen on the catalysts surface. In addition, typical diffraction patterns for the La_2O_3 (PDF 73-2141, marked as ■) and $La(OH)_3$ (PDF 36-1481, marked as ^) were able to be found when the Ni/La molar ratio was less than 4. The presence of $La(OH)_3$ may be due to the reaction between La_2O_3 and H_2O as follows: $La_2O_3 + H_2O \rightarrow La(OH)_3$, because rare-earth oxides are easily hygroscopic when they were exposed to air conditions.[55]

To facilitate comparisons, the percentage compositions of each crystal phase in the Ni$_x$La samples were obtained by Relative Intensity Ratio (RIR) method using JADE 6.5 program as shown in Fig. 7. In terms of the La_2O_3 crystalline phase, the diffraction peaks were also become more intensive with the increasing proportion of La. The peaks of La_2O_3 are quite weak in Ni$_4$La sample and totally disappear in Ni$_5$La sample. This demonstrated that quite low amount of La_2O_3 existed in Ni$_4$La

Table 2 N_2O catalytic performances over S–Ni_xLa samples at 610 K and the specific surface area of Ni_xLa samples

Catalyst	$k/\times 10^{-5}$ mol s^{-1} g^{-1} bar^{-1}	Specific reaction rate/ $\times 10^{-7}$ mol s^{-1} g^{-1} bar^{-1}	Intrinsic reaction rate/ $\times 10^{-8}$ mol s^{-1} m^{-2} bar^{-1}	TOF/ $\times 10^{-5}$ s^{-1}	E_{app}/ kJ mol^{-1}	Specific surface area/m^2 g^{-1}
NiLa	9.74	3.99	2.69	5.87	72.9	14.8
Ni_2La	6.89	2.96	2.01	3.74	124.8	14.8
Ni_3La	12.3	4.73	3.02	6.02	44.8	15.7
Ni_4La	16.6	5.81	3.71	7.74	41.8	15.6
Ni_5La	6.54	4.01	2.63	4.51	112.8	15.2
Ni_6La	7.52	3.21	1.35	3.32	115.7	23.7
Ni_7La	5.33	2.37	0.88	2.22	110.3	27.2
Ni_8La	8.37	3.51	1.28	3.57	145.2	27.4
Ni_9La	7.07	3.04	1.69	2.98	124.4	17.9
$Ni_{10}La$	14.4	5.31	2.14	6.02	69.2	24.9
$La_{0.8}CoO_3$ (ref. 50)		0.20^a	0.84^a		177^b	

[a] Measured at 808 K. [b] Measured at 848 K.

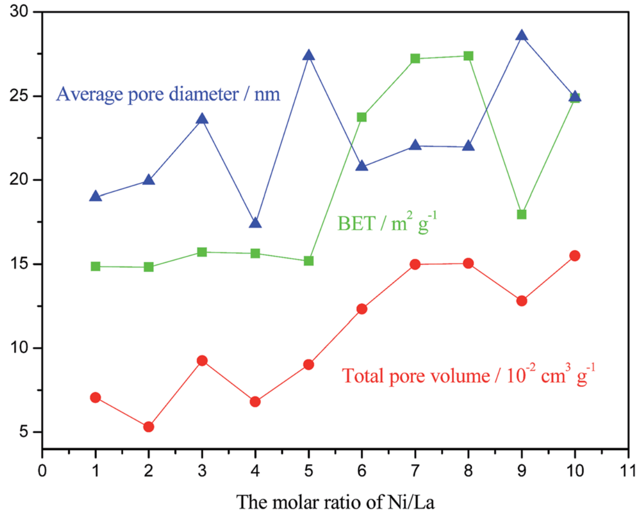

Fig. 5 Textural properties of Ni_xLa samples.

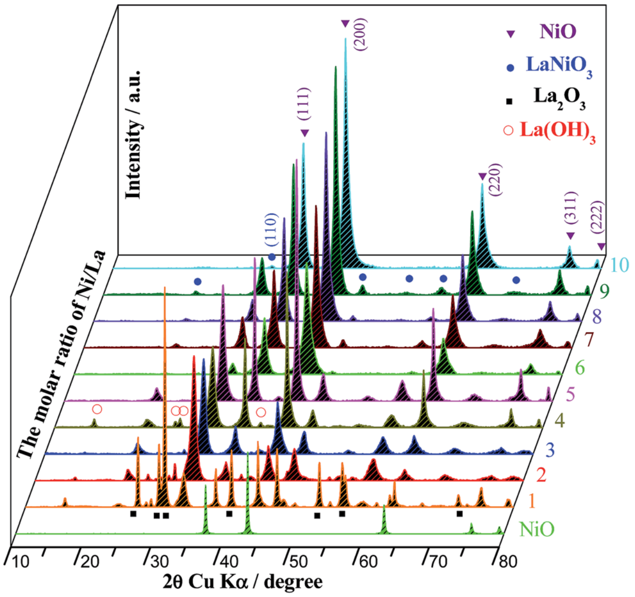

Fig. 6 XRD patterns of the Ni_xLa and pure NiO samples.

sample, which corresponded to the calculated result about 0.5%. When $x = 1$, the percentage composition of La_2O_3 is the highest about 63.8%.

The grain size of NiO in the Ni_4La sample is small (about 15 nm), and the presence of appropriately amount of $LaNiO_3$ structure increased the mobility of O species. Thus, the supported Ni_4La catalyst show the best catalytic performance. Compared to the solid-phase structure and the catalytic activity of the pure NiO sample, the $LaNiO_3$ should be a major active phase for catalytic decomposition of N_2O, especially for the samples of Ni_5La, Ni_6La, Ni_7La, Ni_8La, Ni_9La and $Ni_{10}La$. To the best of our knowledge, the NiO is also a major active component for catalytic decomposition of N_2O, additionally the catalytic activities of the catalysts were not increased with the increased percentage composition of $LaNiO_3$ or NiO, and so the synergy of NiO and $LaNiO_3$ gives rise to catalytic decomposition of N_2O.

To determine whether or not solid solutions were formed in mixed Ni_xLa samples, unit cell parameters were calculated from Bragg's angles, and results are shown in Table 3. For NiLa sample, the unit cell parameters of the $LaNiO_3$ are bigger than others. This may be due to the presence of La_2O_3 promoting the growth of crystalline grain, suggesting that the substitution of La resulted in the distortion of lattice, especially for the Ni_4La sample.

It can be observed that the diffraction peaks of NiO phase shift toward higher angles when compared with the standard JCPDS card as shown in Fig. 8. This may be due to the substitution of La, leading to the distortion of lattice. On the contrary, the diffraction peaks of $LaNiO_3$ phase shift toward lower diffraction angles. As mentioned above, perovskite-type $LaNiO_3$ formed in which La^{III} is substituted by Ni^{III}. Additionally, Wolska *et al.*[56] reported that the charge neutrality could be achieved as substitution of O^{2-} by OH^-, also could cause the distortion of lattice and leading the shift of diffraction angles.

3.4 Micro-morphology

Fig. 9a and b show the microstructure morphology of the Ni_4La sample. The Ni_4La microstructure looks very loose, such as

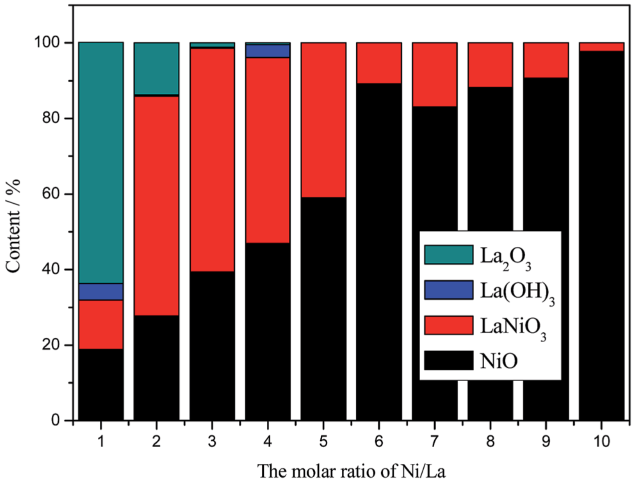

Fig. 7 The percentage compositions of each phase in the Ni_xLa samples.

coral-like structure. It can be seen by ESEM that the equivalent diameter of nano-particle is about 20–25 nm. There are a large number of irregular interstitial holes existed in staggered accumulation of nano-particles. Fig. 9c and d show the surface morphology of bare ceramic honeycomb support. It can be seen that the images of bare ceramic honeycomb presents sheet-like structure. In addition, it is observed that a lot of micro pores are found on the surface of bare ceramic honeycomb. This may be have a great contribution to the activities of Ni–La–O_x supported catalysts. The photographs of supported Ni_4La catalyst are shown in Fig. 9e and f. It can be clearly seen that the presence of Ni–La–O mixed metal oxides, and dispersed homogeneously on the surface of the support.

3.5 H_2-TPR

Asano *et al.*[18] reported that the reducibility enhancement of mixed metal oxides can effectively promote the catalytic activity of N_2O decomposition. The H_2-TPR measurements were performed over the NiLa, Ni_2La, Ni_4La, Ni_6La, Ni_8La and $Ni_{10}La$ samples in order to determine the reducibility and its correlation with catalytic activity. The H_2-TPR profiles of the samples are shown in Fig. 10. The weak peaks appearing at low temperature around 373–573 K are named α peak, which were attributed to the reduction of surface absorbed O species and dispersed NiO. As mentioned above, the ionic radius of Ni^{II} is smaller than La^{III}, and Ni^{II} incorporated into the lattice of La_2O_3 to form $LaNiO_3$ perovskite structure. The formation of $LaNiO_3$ leads to generation of oxygen vacancies, which adsorb oxygen species easily. Therefore, very active oxygen species are formed, which are reduced by H_2 at low temperature.

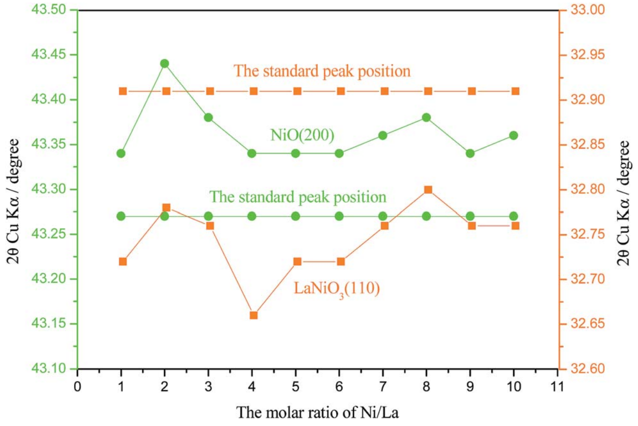

Fig. 8 The diffraction angles of NiO (200) and $LaNiO_3$ (110).

The β peak appearing at around 673 K enhances as Nickel content increases, which corresponds to the reduction of NiO to metallic nickel. The reduction peak of pure NiO sample appeared at around 690 K (data was not shown). This indicated that the reduction ability of Ni_xLa samples were better than bulk NiO sample. Thus, increased the ability of catalysts to accept electronic, and the Ni_xLa catalysts show better catalytic activity. According to the research of Zhou *et al.*,[38] the reduction process of NiO usually follows below: NiO → $Ni^{\delta+}$ → Ni^0, because the crystalline size of pure NiO is big. However, the stepwise reduction of NiO to metallic nickel is not observed in Ni_xLa samples. This illustrates that La additives minimize the crystallite size of NiO. As analyzed above, it can be further implied that the interaction between NiO and $LaNiO_3$ promotes the oxygen mobility and leads to only one main peak observed.

In general, the reduction process of $LaNiO_3$ perovskite oxide follows two consecutive steps expressed by eqn (7) and (8).[57] In the first step about 693 K, Ni^{III} ions stabilized in the $LaNiO_3$ structure are reduced into Ni^{II}, and form an oxygen deficient

Table 3 Unit cell parameters of the phases detected in the Ni_xLa samples as determined by CELREF

		NiLa	Ni_2La	Ni_3La	Ni_4La	Ni_5La
NiO	*a*/Å	4.1784 ± 0.0014	4.1821 ± 0.0130	4.1776 ± 0.0011	4.1791 ± 0.0007	4.1776 ± 0.0003
$LaNiO_3$	*a*/Å	5.5003 ± 0.0099	5.4418 ± 0.0128	5.4604 ± 0.0045	5.4451 ± 0.0122	5.4533 ± 0.0111
	c/Å	6.5940 ± 0.0014	6.5740 ± 0.0050	6.5926 ± 0.0008	6.5646 ± 0.0038	6.5704 ± 0.0135
		Ni_6La	Ni_7La	Ni_8La	Ni_9La	$Ni_{10}La$
NiO	*a*/Å	4.1760 ± 0.0015	4.1794 ± 0.0004	4.1779 ± 0.0011	4.1789 ± 0.0011	4.1777 ± 0.0010
$LaNiO_3$	*a*/Å	5.4739 ± 0.0074	5.4562 ± 0.0102	5.4527 ± 0.0040	5.4300 ± 0.0249	5.4525 ± 0.0109
	c/Å	6.5243 ± 0.0402	6.5599 ± 0.0080	6.5593 ± 0.0016	6.5857 ± 0.0052	6.5718 ± 0.0053

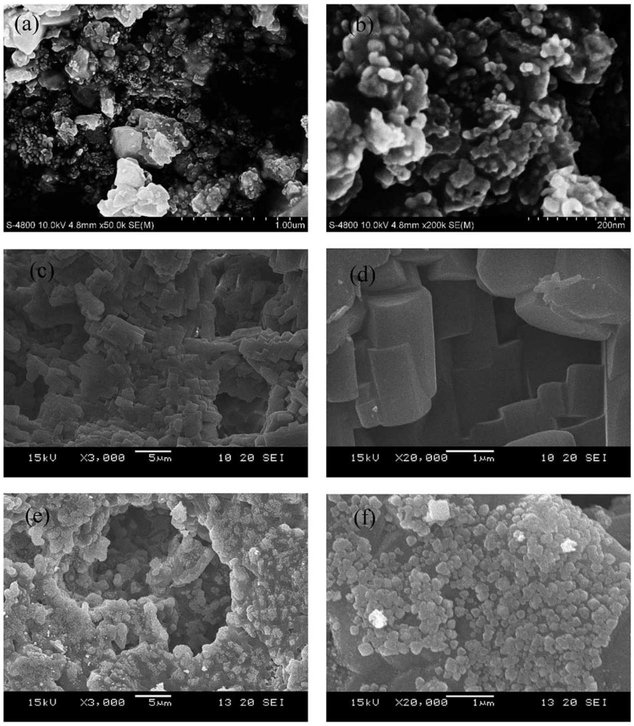

Fig. 9 SEM photograph of Ni_4La mixed metal oxides (a and b); SEM photograph of ceramic honeycomb support (c and d); SEM photograph of supported Ni_4La catalyst (e and f).

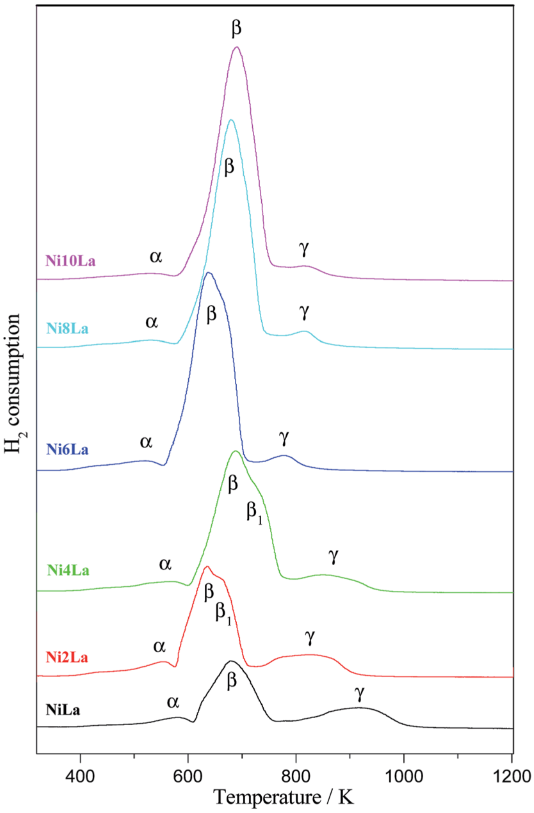

Fig. 10 H_2-TPR profiles of the Ni_xLa samples with different Ni/La molar ratio. Conditions: 10% H_2/Ar, 50 mL min^{-1} and ramping rate of 5 K min^{-1}.

$LaNiO_{2.5}$ structure. In the second step about 823 K, the $LaNiO_{2.5}$ is reduced to metallic nickel and La_2O_3. For the Ni_2La and Ni_4La samples, the shoulder peak is observed and named β_1, indicating that the first reduction peak of $LaNiO_3$ was overlapped with the reduction peak of NiO. With further increase of x values, the β_1 peak disappears and the reduction of NiO species in the Ni_xLa samples presents only one main peak. Furthermore, the H_2 consumption of γ peak attributed to the second reduction step of $LaNiO_3$ decreased with the increase of x values from 2 to 10, which are in accordance with the content of $LaNiO_3$ in Ni_xLa samples calculated by XRD patterns.

$$LaNiO_3 + 1/2H_2 \rightarrow LaNiO_{2.5} + 1/2H_2O \quad (7)$$

(Low-temperature peak)

$$LaNiO_{2.5} + H_2 \rightarrow 1/2La_2O_3 + Ni + H_2O \quad (8)$$

(High-temperature peak)

For NiLa sample, the β_1 peak was not observed. This indicated that only few amount of $LaNiO_3$ exist in the NiLa sample. However, the area of γ peak is larger than others. The appearing of γ peak in NiLa sample must be attributed to the reduction process of other species. According to the study of G. Wrobel *et al.*,[58] when NiO dispersed on the surface of solid solution, strong interaction between free NiO and solid solution is achieved. In the case of NiLa sample, there are large amount of La_2O_3 contained in the sample, there must be of some NiO dispersed on the surface of La_2O_3, so their interaction product may be reduced at higher temperature corresponded to the γ peak.

The peak positions change obviously with the increase of x from 1 to 10. This indicated that a proper amount of $LaNiO_3$ can give rise to significant changes of catalyst structure and thereby enhance them reduction ability. For Ni_4La sample, the onset temperatures of the peaks shift to high values. This may be due to the interaction between NiO and $LaNiO_3$, further indicating that the formation of $LaNiO_3$ solid solution is effective in stabilizing the lower oxidation state of Ni^{II}. Thus, it is easy that the electron transfer from the catalyst to N_2O molecule.

3.6 N_2O-TPD

Catalytic decomposition of N_2O usually is considered as an oxidation–reduction reaction mechanism.[59] This reaction process based on electron transfer follows a three-step mechanism expressed by eqn (9)–(11). Oxides with some local charge donation properties isolated transition metal ions, and leading to more than one valence act as the active site on the surface.[8] In the case of the Ni_xLa samples, Ni^{II} serves as active site in the reaction process. It is reported that the removal of adsorbed oxygen is the rate-determining step of N_2O decomposition. Therefore, N_2O temperature-programmed desorption (N_2O-TPD) experiment was performed for the investigation of the relationship between N_2O catalytic activity and O_2 desorption.

$$N_2O + e^-_{sur} \rightarrow N_2 + O^-_{ads} \quad (9)$$

$$O^-_{ads} + N_2O \rightarrow N_2 + O^-_{2ads} \quad (10)$$

$$2O^-_{ads} \leftrightarrow O_2 + 2e^-_{sur} \quad (11)$$

The decomposition of N_2O over the catalysts left adsorbed O species on the surface during the cooling down step. Fig. 11 shows the N_2O-TPD profiles of the Ni_xLa samples. Several peaks can be seen in the profiles at temperatures from 323 to 873 K. The peak appearing from 373 to 523 K is named α peak, they can be corresponded to desorption of chemically adsorbed oxygen species (O^-, $O_2{}^-$) on the oxygen vacancies, which formed during reaction process. Obviously that desorption peaks shift to higher temperature with Ni content increasing in the Ni_xLa mixed oxide, and The α peak of Ni_4La sample shifts to low temperature, indicating that the mobility and desorption of O_2 are facilitated on the surface of the Ni_4La sample, thus the Ni_4La sample shows the best catalytic activity for N_2O decomposition. Moreover, as the increasing amount of Ni, most of Ni species do not have strong interaction with La, so that the adsorbed O species can be desorbed in the high temperature.

The β peak appeared at around 753 K can be attributed to desorption of subsurface oxygen. In the case of Ni_2La, the temperature of β peak shifts to low value, implied that interaction between O species and metal ions results in desorption of subsurface oxygen easily. According to change the trend of N_2O-TPD profiles, it can be supposed that another γ peak may appear above 873 K. The attribution of the γ desorption peak is the lattice oxygen, namely, the oxygen that is released by the reduction of Ni^{III} according to the following reaction:[60]

$$2Ni^{III} + O^{2-} \rightarrow 2Ni^{II} + V_O + 1/2O_2 \quad (12)$$

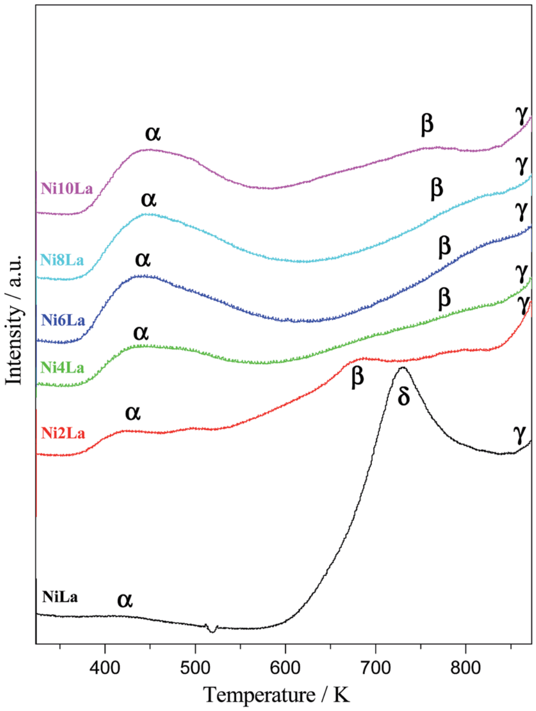

Fig. 11 N_2O-TPD profiles of the Ni_xLa samples with different Ni/La molar ratio.

For NiLa sample, the peak centered at 723 K is named δ peak. Nevertheless, the δ peak was not appearing at other samples. Combined with the results of XRD analysis, the presence of La_2O_3 hindered desorption of oxygen, which in agreement with the result of catalytic activity. As mentioned above, the Ni^{II} acts as the active site for N_2O decomposition. The strength of oxygen bond with active site will directly influence the oxygen mobility. As a result, the desorption of oxygen species can only be achieved at relatively higher temperatures.[17]

3.7 XPS

XPS measurements were carried out to examine the surface electronic state of the Ni_4La sample. Fig. 12 and 13 presented the spectra of Ni 2p, La 3d and O 1s core-level, respectively. The binding energies of Ni $2p_{1/2}$, $2p_{3/2}$, La $3d_{3/2}$, $3d_{5/2}$ and O 1s determined by XPS are summarized in Table 4. The Ni/La atomic ratio was determined by the element relative sensitivity factor (RSF) method, and calculated using. The calculation result was 3.58 (fresh catalyst) and 4.42 (treated by N_2O), which were close to the design Ni/La atomic ratio of 4.

$$C_A = \frac{I_A/F_A}{\sum I/F} \quad (13)$$

Fig. 12 shows the peak fitting results of Ni 2p and La 3d binding energies, which are determined by peak fitting through XPSPeak4.1. As we known that the La $3d_{3/2}$ peak overlap Ni $2p_{3/2}$ peak,[61] and the La 3d core level split into $3d_{5/2}$ and $3d_{3/2}$ components due to a spin–orbit interaction. Additionally each

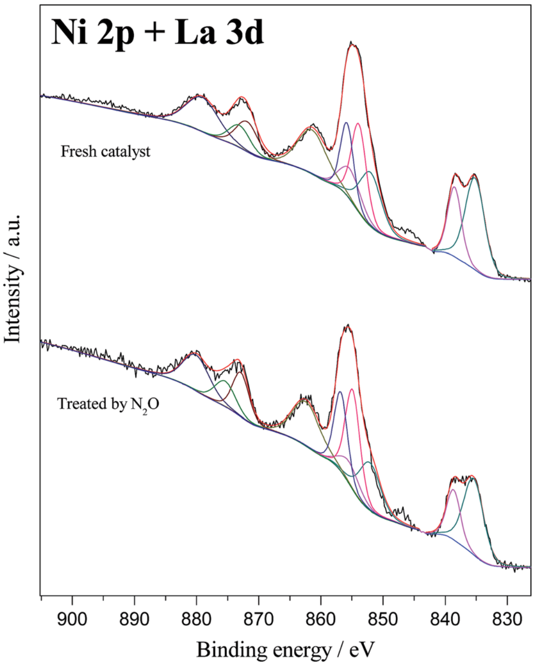

Fig. 12 Ni 2p and La 3d core level spectra of the Ni_4La sample at two conditions, (1) fresh catalyst and (2) after exposure of N_2O (N_2 balance).

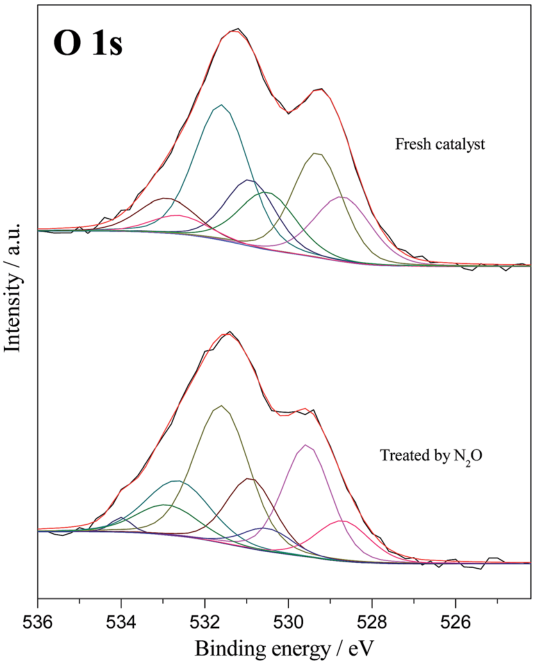

Fig. 13 O 1s core level spectra of the Ni_4La samples at two conditions: (1) fresh catalyst and (2) after exposure of N_2O (N_2 balance).

Table 4 Fitting results of Ni 2p, La 3d and O 1s photoelectron spectra of Ni_4La sample

Peak parameters				Peak identification		
Fresh Ni_4La catalyst		Treated by N_2O				
BE (eV)	FWHM	BE (eV)	FWHM	Species	Line	Assignment
871.9	4.17	871.9	4.13	NiO	$2p_{1/2}$	Core
853.9	2.85	853.9	2.78	NiO	$2p_{3/2}$	Core
873.1	4.04	873.2	3.98	Ni_2O_3	$2p_{1/2}$	Core
855.8	2.47	855.8	2.51	Ni_2O_3	$2p_{3/2}$	Core
861.4	5.43	861.4	5.22			Satellite
879.1	6.12	879.1	5.04			Satellite
852	4.1	851.9	4.04	La_2O_3	$3d_{3/2}$	Core
855.3	4.08	855.2	3.94			Shake up
835.2	3.69	835.2	3.8	La_2O_3	$3d_{5/2}$	Core
838.5	2.6	838.4	2.6			Shake up
531.6	1.52	531.6	1.82	Ni^{II}–O	1s	Core
529.3	1.4	529.5	1.36	La–O	1s	Core
530.9	1.41	530.9	1.59	Ni^{III}–O	1s	Core
532.6	1.6	532.6	2.08	O ads	1s	Core
528.7	1.6	528.7	1.49	O^{2-}	1s	Core
530.5	1.6	530.5	1.4	O^-	1s	Core
532.9	1.59	532.9	1.75	H_2O/OH	1s	Core
		534	0.58	Ads-O_2	1s	Core

line split to main line ($3d^04f^0$ final state configuration) and a satellite line ($3d^04f^1L$ final state configuration).[62,63] For the fresh and used Ni_4La samples, the peaks of Ni 2p appearing at 871.9 eV and 853.9 eV belong to Ni^{II} core-level. Moreover, shake up satellite peaks of Ni^{II} appear at 861.4 eV and 879.1 eV, respectively. This indicates that the presence of NiO on the catalyst surface. The binding energies of 873.1 eV and 855.8 eV correspond to Ni^{III} $2p_{1/2}$ and Ni^{III} $2p_{3/2}$ core-level, which related to the formation of $LaNiO_3$ on the surface. The percentage content of Ni^{III} is about 25%. These results demonstrated that only NiO and $LaNiO_3$ species were present on the catalyst surface, which are similar to XRD results.

The spectra were not significantly different among the samples. However, a small change was observed over a variety of peaks that fitted the spectra. This change may be caused by sample preparation during the experiments. Such change of fitting peaks was also observed by Mark C. Biesinger.[64] If the samples contain only a small amount of Ni^{II}, then the spectrum is very well defined, but if the degree of reduction of Ni^{III} to Ni^{II} is high, then the binding energy of Ni $2p_{3/2}$ would shift to low values. For the Ni_4La sample, the binding energy of Ni $2p_{3/2}$ was not shifted after pretreatment by N_2O at 723 K. This indicates that the Ni^{II} is not oxidized by N_2O treatment, further suggesting that the Ni^{II} and oxygen vacancies are more stable during the N_2O decomposition process. As a result, they are able to enhance desorption and mobility of the oxygen, which is the rate-determining step in such a reaction. This result is in great agreement with the analysis of activity and stability.

The core levels of O 1s spectra for two samples are shown in Fig. 13. The O 1s peaks are complex and this result indicates that the presence of more than one type of oxygen species in the surface. The peak appearing at 529.3 eV can be ascribed to lattice O^{2-} anion in lanthanum oxides.[65] According to the literature, the chemical boding in $LaNiO_3$ was not purely ionic, but exhibited covalent (Ni–O and La–O) and metallic (Ni–O–Ni) parts that can explain the presence of two different oxides in the fresh sample.[66] The peaks appearing at 530.5 eV and 534 eV in the used sample can be ascribed to adsorbed O^- and O_2, which were not found in the fresh sample. This indicates that O^- and O_2 form during the N_2O decomposition process, which in agreement with the result of N_2O-TPD. In addition, if Ni^{II} anion was oxidized to Ni^{III} after pretreatment by N_2O, the peak at 531.6 eV would start to vanish. This factor further confirms that the Ni^{II} is not oxidized by N_2O treatment. As mentioned above, the rare earth oxides are easily hygroscopic when they are exposed to atmospheric conditions.[55] The peak appearing at 532.9 eV can be attributed to the adsorbed water species at the surface. Future studies are needed to evaluate the catalyst activity in the presence of O_2 and H_2O.

4. Discussion

So far, several reaction mechanisms for N_2O decomposition have been proposed by different researchers.[10,21,59] It is generally accepted that the reaction is an oxidation–reduction process. The surface oxygen vacancies (V_O) and metal ions act as the active center, and N_2O act as an oxidizing agent in the reducing step. The S–Ni_xLa samples exhibit higher catalytic activity than that of pure NiO supported catalyst. This may be due to the presence of $LaNiO_3$ structure which gives rise to the oxygen non-stoichiometry in the surface. Based on the results obtained, we proposed a possible reactions mechanism as presented in Scheme 1. To the best of our knowledge, N_2O molecular is linear structure and it can be adsorbed either through O or N ends.[18] As for the case of coordination on N end, the N–O bond order increases and the N–N bond decreases. As a result, NO or NO_2 would be the byproducts for N_2O decomposition. However, we have not yet detected NO or NO_2 species in XPS and GC analysis. Therefore, the coordination takes place on the O end, and product is nitrogen. As is shown in Scheme 1, N_2O deposits on the active centers such as oxygen vacancies and Ni^{II} with the O atom expressed in eqn (14)–(17). This process involved a transient N_2O^- specie that formed by the electron from the d_{xy} donor orbital toward $3\pi^*$ acceptor orbital of the N_2O. Subsequently dissociative chemisorption of N_2O molecule on the surface active center and release of N_2 expressed by eqn (16) and (17). The XPS results also confirm the presence of O^{2-} and O^- species.

$$Ni^{II} + N_2O \rightarrow Ni^{II}\cdots ONN \tag{14}$$

$$V_O + N_2O \rightarrow V_O\cdots ONN \tag{15}$$

$$Ni^{II}\cdots ONN \rightarrow Ni^{III}\cdots O^- + N_2 \tag{16}$$

$$V_O\cdots ONN \rightarrow V_O\cdots O^{2-} + N_2 \tag{17}$$

In terms of the activity result, the presence of $LaNiO_3$ increased the catalytic activity of catalyst. This may be due to the presence of Ni^{III} facilitated the Ni^{III} (Ni^{III}–O^-) reduced to Ni^{II}, and oxygen removed promptly. However, the activity was not increased with the increased amount of $LaNiO_3$. The removal of adsorbed oxygen is the rate-determining step for N_2O decomposition. After the above steps, the formation of O_2 in two ways: (i) the two neighboring O^- species combined with each other and Ni^{III} was reduced into Ni^{II} expressed by eqn (18); (ii) the O^{2-} in vacancy sites interaction with another N_2O molecule expressed by eqn (19). These steps involved the electron migration from O^- or O^{2-} species to the surface. The results of N_2O-TPD and XPS clearly support this hypothesis as discussed.

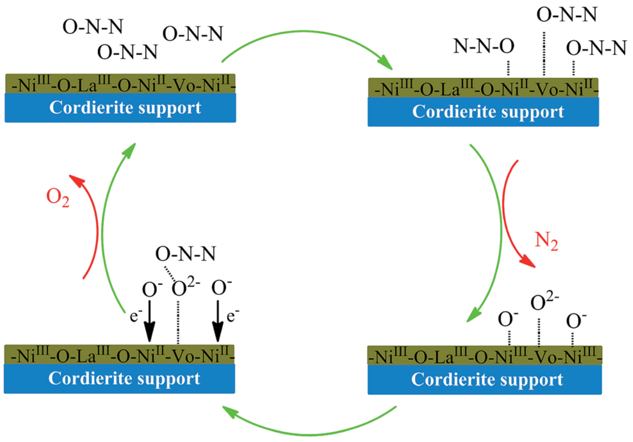

Scheme 1 Catalytic mechanism for N_2O decomposition over the supported Ni_xLa catalysts.

$$2Ni^{III}\cdots O^- \rightarrow 2Ni^{II} + O_2 \tag{18}$$

$$V_O\cdots O^{2-} + N_2O \rightarrow V_O + O_2 + N_2 \tag{19}$$

In summary, the $LaNiO_3$ enhanced desorption and migration of oxygen, and resulted in high catalytic activity for N_2O decomposition over the Ni_xLa supported catalysts.

5. Conclusions

This work has been confirmed that the supported Ni–La–O_x complex oxides are promising catalyst system for N_2O decomposition. The S–Ni_4La catalyst obtains full N_2O conversion at 708 K and displays perfect stability in N_2O decomposition. The NiO and $LaNiO_3$ are major active solid-phase structures for catalytic decomposition of N_2O, and the promotional mechanism is that the synergetic action between NiO and $LaNiO_3$ promotes oxygen mobility and desorption, and stabilizes the active site of Ni^{II}. Future studies are needed to evaluate catalytic performance in the presence of O_2 and H_2O.

Acknowledgements

This work was supported by the National Key Technology Support Program (no. 2012BAE01B03), the National Natural Science Foundation of China (no. 21106071, 51272105), the New Teachers' Fund for Doctor Stations Sponsored by the Ministry of Education of China (no. 20113221120004), the Research Subject of Environmental Protection Department of Jiangsu Province of China (no. 2012016), the Jiangsu Provincial Science and Technology Supporting Program (no. BE2013718, BE2011184), the Priority Academic Program Development of Jiangsu Higher Education Institutions (PAPD), and Program for Changjiang Scholars and Innovative Research Team in University (no. IRT1146).

References

1 P. Crutzen and C. Howard, *Pure Appl. Geophys.*, 1978, **116**, 497–510.
2 M. Kavanaugh, *Atmos. Environ.*, 1987, **21**, 463–468.
3 G. Centi, S. Perathoner and F. Vazzana, *CHEMTECH*, 1999, **29**, 48–55.
4 J. Perez-Ramirez, F. Kapteijn, K. Schoffel and J. A. Moulijn, *Appl. Catal., B*, 2003, **44**, 117–151.
5 H. Rodhe, *Science*, 1990, **248**, 1217–1219.
6 M. A. Wojtowicz, J. R. Pels and J. A. Moulijn, *Fuel Process. Technol.*, 1993, **34**, 1–71.
7 J. C. Kramlich and W. P. Linak, *Prog. Energy Combust. Sci.*, 1994, **20**, 149–202.
8 F. Kapteijn, J. RodriguezMirasol and J. A. Moulijn, *Appl. Catal., B*, 1996, **9**, 25–64.
9 G. Centi, A. Galli, B. Montanari, S. Perathoner and A. Vaccari, *Catal. Today*, 1997, **35**, 113–120.
10 S. Kumar, A. Vinu, J. Subrt, S. Bakardjieva, S. Rayalu, Y. Teraoka and N. Labhsetwar, *Catal. Today*, 2012, **1998**, 125–132.

11 K. Yuzaki, T. Yarimizu, K. Aoyagi, S. Ito and K. Kunimori, *Catal. Today*, 1998, **45**, 129–134.

12 J. Haber, M. Nattich and T. Machej, *Appl. Catal., B*, 2008, **77**, 278–283.

13 V. G. Komvokis, G. E. Marnellos, I. A. Vasalos and K. S. Triantafyllidis, *Appl. Catal., B*, 2009, **89**, 627–634.

14 H. Beyer, J. Emmerich, K. Chatziapostolou and K. Koehler, *Appl. Catal., A*, 2011, **391**, 411–416.

15 S. S. Kim, S. J. Lee and S. C. Hong, *Chem. Eng. J.*, 2011, **169**, 173–179.

16 F. J. Perez-Alonso, I. Melian-Cabrera, M. L. Granados, F. Kapteijn and J. L. G. Fierro, *J. Catal.*, 2006, **239**, 340–346.

17 L. Xue, C. Zhang, H. He and Y. Teraoka, *Appl. Catal., B*, 2007, **75**, 167–174.

18 K. Asano, C. Ohnishi, S. Iwamoto, Y. Shioya and M. Inoue, *Appl. Catal., B*, 2008, **78**, 242–249.

19 N. Pasha, N. Lingaiah, P. S. S. Reddy and P. S. Prasad, *Catal. Lett.*, 2009, **127**, 101–106.

20 R. Amrousse and T. Katsumi, *Catal. Commun.*, 2012, **26**, 194–198.

21 H. Zhou, Z. Huang, C. Sun, F. Qin, D. Xiong, W. Shen and H. Xu, *Appl. Catal., B*, 2012, **125**, 492–498.

22 P. Pomonis, D. Vattis, A. Lycourghiotis and C. Kordulis, *J. Chem. Soc., Faraday Trans. 1*, 1985, **81**, 2043–2051.

23 A. Dandekar and M. A. Vannice, *Appl. Catal., B*, 1999, **22**, 179–200.

24 A. K. Ladavos and T. V. Bakas, *React. Kinet. Catal. Lett.*, 2001, **73**, 229–235.

25 G. Giecko, T. Borowiecki, W. Gac and J. Kruk, *Catal. Today*, 2008, **137**, 403–409.

26 T. Gaidei, N. Pillet, V. Sadov, M. Strukova, S. Filatov, E. Khaustova and N. Yaroshenko, *Russ. J. Appl. Chem.*, 2010, **83**, 1154–1158.

27 R. S. da Cruz, A. J. S. Mascarenhas and H. M. C. Andrade, *Appl. Catal., B*, 1998, **18**, 223–231.

28 R. Joyner and M. Stockenhuber, *J. Phys. Chem. B*, 1999, **103**, 5963–5976.

29 L. Li, Q. Shen, J. Yu, J. Li, Z. Hao and Z. P. Xu, *Catal. Commun.*, 2008, **9**, 1745–1748.

30 P. K. Roy, R. Prins and G. D. Pirngruber, *Appl. Catal., B*, 2008, **80**, 226–236.

31 A. Ates, A. Reitzmann and G. Waters, *Appl. Catal., B*, 2012, **119**, 329–339.

32 J. Y. Wang, H. A. Xia, X. H. Ju, F. T. Fan, Z. C. Feng and C. Li, *Chin. J. Catal.*, 2013, **34**, 876–888.

33 K. S. Chang, H. Song, Y. S. Park and J. W. Woo, *Appl. Catal., A*, 2004, **273**, 223–231.

34 L. Obalová, K. Jirátová, F. Kovanda, K. Pacultová, Z. Lacný and Z. Mikulová, *Appl. Catal., B*, 2005, **60**, 289–297.

35 L. Obalová, K. Pacultová, J. Balabánová, K. Jirátová, Z. Bastl, M. Valášková, Z. Lacný and F. Kovanda, *Catal. Today*, 2007, **119**, 233–238.

36 V. K. Tzitzios and V. Georgakilas, *Chemosphere*, 2005, **59**, 887–891.

37 P. Reddy, N. Pasha, M. Chalapathi Rao, N. Lingaiah, I. Suryanarayana and P. Sai Prasad, *Catal. Commun.*, 2007, **8**, 1406–1410.

38 H. B. Zhou, P. L. Hu, Z. Huang, F. Qin, W. Shen and H. L. Xu, *Ind. Eng. Chem. Res.*, 2013, **52**, 4504–4509.

39 N. Russo, D. Mescia, D. Fino, G. Saracco and V. Specchia, *Ind. Eng. Chem. Res.*, 2007, **46**, 4226–4231.

40 E. Iwanek, K. Krawczyk, J. Petryk, J. W. Sobczak and Z. Kaszkur, *Appl. Catal., B*, 2011, **106**, 416–422.

41 A. Gervasini, P. Carniti and S. Bennici, *React. Kinet., Mech. Catal.*, 2012, **105**, 53–67.

42 S. Liu, Y. Cong, C. Kappenstein and T. Zhang, *Chin. J. Catal.*, 2012, **33**, 907–913.

43 Y. Wu, C. Dujardin, P. Granger, C. Tiseanu, S. Sandu, V. Kuncser and V. I. Parvulescu, *J. Phys. Chem. C*, 2013, **117**, 13989–13999.

44 Z. Lan, S. C. Zhang, L. Q. Wang and C. H. Liu, *Ind. Catal.*, 2002, **10**, 54–56.

45 Y. Wang, J. Zhang, J. Zhu, J. Yin and H. Wang, *Energy Convers. Manage.*, 2009, **50**, 1304–1307.

46 CELREF unit-cell refinement software for Windows by Laugier and Bochu, http://www.ccp14.ac.uk/.

47 A. Heyden, B. Peters, A. T. Bell and F. J. Keil, *J. Phys. Chem. B*, 2005, **109**, 1857–1873.

48 G. D. Pirngruber, P. K. Roy and R. Prins, *J. Catal.*, 2007, **246**, 147–157.

49 N. Liu, R. Zhang, B. Chen, Y. Li and Y. Li, *J. Catal.*, 2012, **294**, 99–112.

50 Y. Wu, X. Ni, A. Beaurain, C. Dujardin and P. Granger, *Appl. Catal., B*, 2012, **125**, 149–157.

51 R. J. Madon and M. Boudart, *Ind. Eng. Chem. Fundam.*, 1982, **21**, 438–447.

52 R. Weber, M. Plinke, Z. T. Xu and M. Wilken, *Appl. Catal., B*, 2001, **31**, 195–207.

53 R. Klaewkla, M. Arend and W. F. Hoelderich, *Mass Transfer-Advanced Aspects*, 2011, pp. 668–684.

54 S. Parres-Esclapez, I. Such-Basañez, M. J. Illán-Gómez, C. Salinas-Martínez de Lecea and A. Bueno-López, *J. Catal.*, 2010, **276**, 390–401.

55 A. De Asha, J. Critchley and R. Nix, *Surf. Sci.*, 1998, **405**, 201–214.

56 E. Wolska and U. Schwertmann, *Z. Kristallogr*, 1989, **189**, 223–237.

57 J. Requies, M. A. Cabrero, V. L. Barrio, M. B. Guemez, J. F. Cambra, P. L. Arias, F. J. Perez-Alonso, M. Ojeda, M. A. Pena and J. L. G. Fierro, *Appl. Catal., A*, 2005, **289**, 214–223.

58 G. Wrobel, M. P. Sohier, A. D'Huysser, J. P. Bonnelle and J. P. Marcq, *Appl. Catal., A*, 1993, **101**, 73–93.

59 P. Pietrzyk, F. Zasada, W. Piskorz, A. Kotarba and Z. Sojka, *Catal. Today*, 2007, **119**, 219–227.

60 Z. Zhao, X. Yang and Y. Wu, *Appl. Catal., B*, 1996, **8**, 281–297.

61 J. F. Moulder, J. Chastain and R. C. King, *Handbook of X-ray photoelectron spectroscopy: a reference book of standard spectra for identification and interpretation of XPS data*, Physical Electronics, Eden Prairie, MN, 1995.

62 D. F. Mullica, C. K. C. Lok, H. O. Perkins and V. Young, *Phys. Rev. B: Condens. Matter Mater. Phys.*, 1985, **31**, 4039–4042.

63 C. Suzuki, J. Kawai, M. Takahashi, A.-M. Vlaicu, H. Adachi and T. Mukoyama, *Chem. Phys.*, 2000, **253**, 27–40.

64 M. C. Biesinger, B. P. Payne, A. P. Grosvenor, L. W. Lau, A. R. Gerson and R. S. C. Smart, *Appl. Surf. Sci.*, 2011, **257**, 2717–2730.

65 T. L. Barr, *J. Phys. Chem.*, 1978, **82**, 1801–1810.

66 A. Y. Dobin, K. Nikolaev, I. Krivorotov, R. Wentzcovitch, E. D. Dahlberg and A. Goldman, *Phys. Rev. B: Condens. Matter Mater. Phys.*, 2003, **68**, 113408.